



# On the role of seamounts in upwelling deep-ocean waters through turbulent mixing

Ali Mashayek<sup>a,1</sup> , Jonathan Gula<sup>b,c</sup> , Lois E. Baker<sup>d</sup> , Alberto C. Naveira Garabato<sup>e</sup>, Laura Cimolif , James J. Riley<sup>g</sup> , and Casimir de Lavergne<sup>h</sup>

Affiliations are included on p. 9.

Edited by Michael Manga, University of California, Berkeley, CA; received December 21, 2023; accepted May 8, 2024

Turbulent mixing in the ocean exerts an important control on the rate and structure of the overturning circulation. However, the balance of processes underpinning this mixing is subject to significant uncertainties, limiting our understanding of the overturning's deep upwelling limb. Here, we investigate the hitherto primarily neglected role of tens of thousands of seamounts in sustaining deep-ocean upwelling. Dynamical theory indicates that seamounts may stir and mix deep waters by generating lee waves and topographic wake vortices. At low latitudes, stirring and mixing are predicted to be enhanced by a layered vortex regime in the wakes. Using three realistic regional simulations spanning equatorial to middle latitudes, we show that layered wake vortices and elevated mixing are widespread around seamounts. We identify scalings that relate mixing rate within seamount wakes to topographic and hydrographic parameters. We then apply such scalings to a global seamount dataset and an ocean climatology to show that seamount-generated mixing makes an important contribution to the upwelling of deep waters. Our work thus brings seamounts to the fore of the deep-ocean mixing problem and urges observational, theoretical, and modeling efforts toward incorporating the seamounts' mixing effects in conceptual and numerical ocean circulation models.

seamounts | ocean | mixing | upwelling | circulation

Turbulence at centimeter scales plays a pivotal role in shaping the overturning circulation of the deep ocean (1, 2), as well as the ocean's capacity to distribute and store climate-critical tracers (3, 4). As dense, deep water masses flow away from their high-latitude formation regions, small-scale turbulence induces mixing with surrounding layers, leading to a net transfer of water across isopycnals. These transfers regulate the rate and structure of deep-ocean overturning (5–7) and, in so doing, influence the oceanic inventories and turnover time scales of heat, carbon, and other important biogeochemical substances.

Decades of research in ocean mixing have brought a solid understanding of the key energy sources of turbulent mixing (winds, tides, and geothermal heating through the seafloor) (1, 8), and of a wide range of mechanisms of small-scale turbulence generation (9, 10). However, several major knowledge gaps remain. Possibly chief among these is the uncertain role of turbulent processes near the ocean's bottom boundary (11, 12). These processes have been argued to potentially account for the bulk of deep-ocean upwelling (1, 2) but, with few targeted observations, comparatively little is known about their nature and large-scale impacts.

Most past investigations of turbulent mixing near the bottom boundary have examined contributions from either the breaking of internal waves (following the waves' generation, reflection, or scattering at the boundary; see ref. 9 for a recent review), or a range of complex nonwave processes in topographically constrained canyons and passages (e.g., hydraulic jumps at sills) (13, 14). More recently, the focus has shifted increasingly to a distinct class of phenomena underpinning near-boundary mixing: submesoscale instabilities (15–20). These instabilities develop as quasi-geostrophic flows over sloping topography generate a reversal in the sign of potential vorticity (a conserved property of geophysical fluids that can only be changed by frictional and diabatic processes) near the boundary and induce overturning motions that restore stability by mixing boundary and off-boundary waters. Intense near-bottom mixing by submesoscale instabilities has been documented in some regions with energetic mesoscale motions [e.g., the Gulf Stream (16) or a deep western boundary current in the Scotia Sea (18)], suggesting that these instabilities may be widely active mixing agents.

## Significance

This research uncovers the crucial role of seamounts, underwater mountains, in influencing deep-ocean circulation. Seamounts stir and mix deep waters by generating waves and vortices, particularly in low-latitude regions. This study employs realistic simulations and identifies key parameters affecting mixing rates around seamounts. Applying these findings to a global seamount dataset, the research demonstrates that seamount-generated mixing significantly contributes to the upwelling of deep waters. This finding challenges previous understanding and emphasizes the need to incorporate seamount effects in ocean circulation models. By shedding light on this previously overlooked aspect, the study paves the way for more accurate representations of ocean dynamics and ultimately advances our comprehension of Earth's complex climate system.

The authors declare no competing interest.

This article is a PNAS Direct Submission.

Copyright © 2024 the Author(s). Published by PNAS. This article is distributed under Creative Commons Attribution-NonCommercial-NoDerivatives License 4.0 (CC BY-NC-ND).

<sup>1</sup>To whom correspondence may be addressed. Email: am3158@cam.ac.uk.

This article contains supporting information online at <https://www.pnas.org/lookup/suppl/doi:10.1073/pnas.2322163121/-DCSupplemental>.

Published June 25, 2024.

Yet, as common as these instabilities might be, fresh theoretical advances emphasize the potential prevalence of a largely neglected, more generic form of mesoscale flow-topography interaction, which encompasses and broadens most scenarios of submesoscale instability development: the generation of topographic wakes (21). These wakes are produced when the highly sheared near-boundary flow separates from sloping topography and moves into the oceanic interior (21). Flow separation need not always be associated with a reversal in the sign of potential vorticity close to the boundary but may be readily enabled by the boundary's geometry (15) or the background mesoscale strain field (22). Upon escaping the boundary's constraint, the separated, sheared flow undergoes a variety of instabilities, which lead to both elevated turbulent mixing in the wake (16, 23–25) and the generation of submesoscale vortical filaments (15, 26, 27).

Where, then, might we expect topographic wakes to induce vigorous turbulent mixing in the deep ocean? Although wake generation can potentially occur at various types of sloping topography, the most common form of such topography is provided by isolated volcanic seamounts—of which some tens to hundreds of thousands with heights of hundreds of meters or taller are estimated to exist (28–30). Thus, in this work, we combine the latest developments in our theoretical understanding of wake generation with a global seamount census to perform a baseline assessment of the role of topographic wakes in sustaining deep-ocean mixing and upwelling. This allows us to address the fundamental question posed initially by Munk and Wunsch (8): “Are seamounts and islands the stirring rods of the oceans?”

## Global Seamount Census

Our analysis is founded on the seamount dataset of Kim and Wessel (31, hereafter KW11), which includes ~25,000 seamounts with heights over 100 m in areas away from continental margins. Approximately 8,500 of these seamounts are taller than 1 km. KW11 predict that their database likely underestimates the global inventory of seamounts by nearly a factor of two; this is confirmed by Gevorgian et al. (32), who updated the total number to 43,454 seamounts. Thus, the KW11 database is conservative, as it includes a significantly lower number of seamounts than other predictions. For example, Wessel et al. (28) reported more than 100,000 seamounts with heights exceeding 1 km, and speculated that there are probably 25 million seamounts taller than 100 m. Similarly, Yesson et al. (29) reported ~140,000 seamounts with peak heights between 500 m and 1 km, and ~33,500 seamounts taller than 1 km. The KW11 data incorporate corrections for the ambiguity in gravity signals due to small seamounts and for the overlap with abyssal hills, which are typically 100 m high on a horizontal scale <10 km, and most prevalent along mid-ocean ridges (33). As a result, seamounts captured by the KW11 data are distinct from abyssal hills and correspond instead to active or extinct undersea volcanoes (of isolated or combination conical shapes) with heights over 100 m. It is worth noting that in the realistic simulations performed in this study, each using high-resolution bathymetry derived from multibeam surveys, there are multiple examples of seamounts that are not found in the KW11 seamount census, emphasizing the conservative seamount count of KW11. Fig. 1B shows the global distribution of the KW11 seamounts, colored by their height. For reference, the seafloor depth is shown in Fig. 1A.

## Flow Around a Seamount

A flow past a seamount generates a turbulent topographic wake with patches of both cyclonic and anticyclonic vorticity, leading to instabilities and formation of submesoscale coherent vortices with either sign of vorticity in the wake of the seamount (26, 27, 36, 37). While two-dimensional (2D) wake flow past a cylinder is a classic problem in fluid mechanics, the description of 3D seamount wakes in a rotating density-stratified ocean is a recently attacked and more complex problem. The impacts of rotation and stratification on wake dynamics can be encapsulated in two dimensionless numbers: the Rossby number  $Ro = \frac{U}{fD}$ , and the Froude number  $Fr = \frac{U}{NH}$ , where  $U$  is the horizontal velocity,  $f$  is the Coriolis frequency,  $N$  is the buoyancy frequency,  $H$  is the height of the seamount, and  $D$  is the diameter of the seamount at its mid-height. The Froude number gives the ratio of the energetically possible amplitude of vertical fluid displacement to the seamount height. A small Froude number ( $Fr < 1$ ) implies that the flow skirts most of the height of the seamount and leads predominantly to the generation of wake vortices, although lee wave generation still occurs from the top portion of the seamount, which has effective height  $\sim U/N$  (Fig. 1D) (38, 39). In contrast, a large Froude number ( $Fr > 1$ ) describes a lee wave-dominated regime with most of the flow directed over rather than around the seamount, resulting in relatively stronger generation of topographic lee waves than topographic wakes (39). We note that there exists extensive literature on flow over mountains in the atmospheric context (40, 41), but such flows often correspond to higher Froude numbers as compared to the oceanic flows over seamounts, and thus, the dynamics are dominated by lee wave generation, which is not our focus herein.

The vertical structure of wake vortices has been found to further depend on the ratio of Rossby and Froude numbers, expressed by the Burger number  $Bu = (Ro/Fr)^2 = (\frac{NH}{fD})^2$  (26, 42). The Burger number can also be viewed as the (squared) ratio of an effective Rossby deformation radius  $R_D \sim NH/f$  (where the seamount height  $H$  replaces the seafloor depth as the relevant vertical length scale) and the mid-height seamount diameter  $D$ . Small  $Bu$  values are associated with vertically coherent vortices (with horizontal scale set by the deformation radius), whereas large  $Bu$  values characterize layered vortices (with horizontal scale at a given depth set by the local seamount diameter at that depth) (26)—see Fig. 1D. This latter case carries important implications for the generation of small-scale turbulence within the wakes, due to the strong vertical shear between the vortices' layers (27, 42). For small and moderate values of  $Ro$  and  $Bu$ , the turbulent mixing occurs predominantly in the anticyclonic region of the wake due to centrifugal (or inertial) instability (16, 23), eventually enhanced by the contribution of secondary wave emission from the unstable wake (21) and by the generation and trapping of near-inertial waves (24). However, large  $Bu$  and order one  $Ro$  values imply a transition to a more effective stratified turbulence regime driven by three-dimensional vertical shear instabilities in the wake (43). Hence, low-latitude topographic wakes may be expected to be particularly effective at generating small-scale turbulence, as the equatorward-decreasing  $f$  results in wake structures that are more vertically sheared and more susceptible to instability (43). The dependence on  $Bu$  of dynamical regimes of flow impingement on seamounts outlined here has been recently explored and corroborated with large eddy simulations (39, 42).

In this work, we set aside the lee wave radiation regime, which, despite its regional significance, has been investigated within

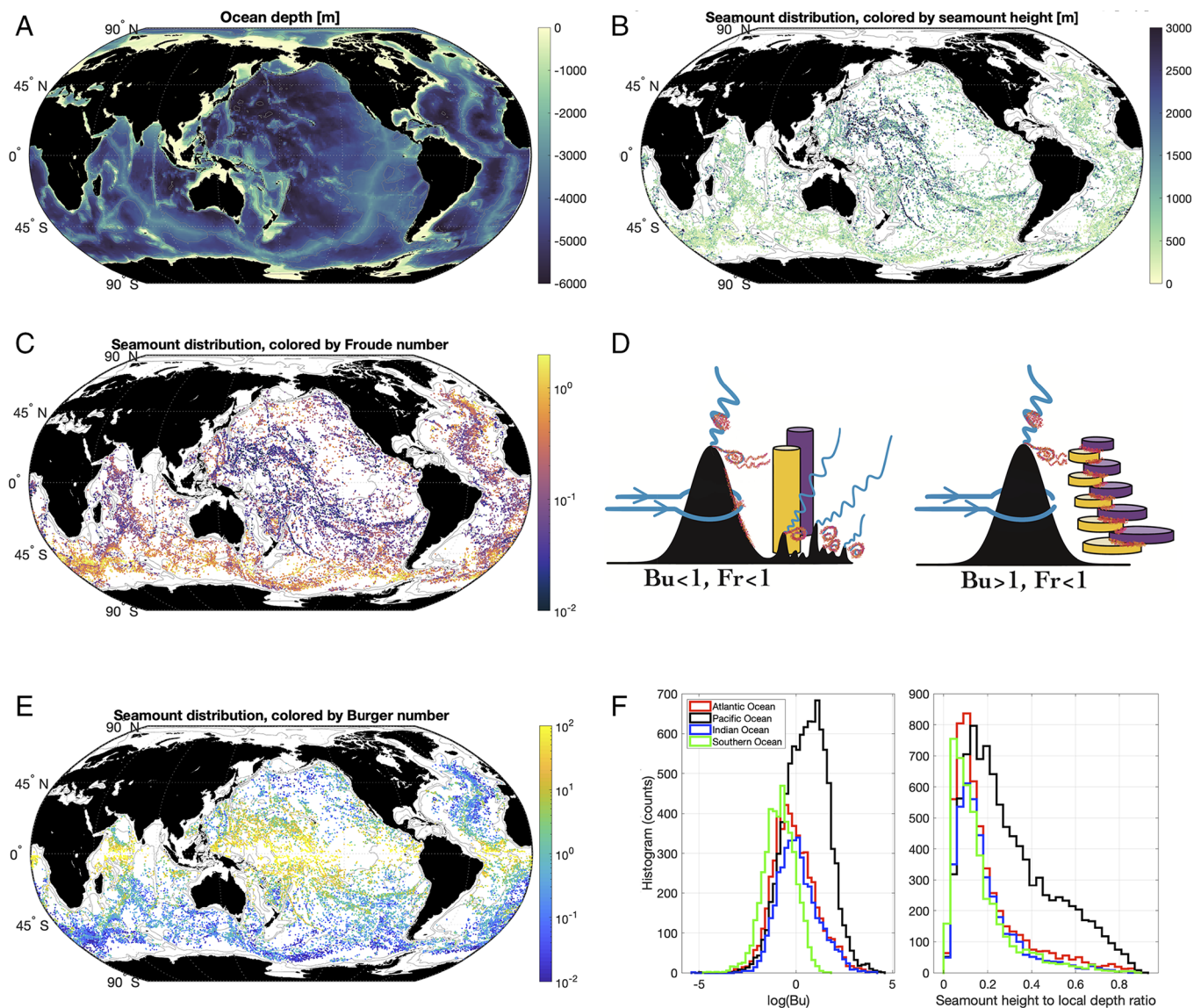


**Fig. 1.** (A) Ocean depth. (B) Global distribution of seamounts (from ref. 31), composed of ~25,000 seamounts. (C) Same as panel (B), but colored based on the seamount Froude number. (D) A schematic summarizing the various dynamical paradigms of flow around seamounts as a function of Burger and Froude numbers. (E) Same as panel (B), but colored based on the seamount Burger number. (F) Histograms of seamount counts based on (Left) their Burger numbers and (Right) their height to basal-depth ratios, divided into different basins. A map of Rossby number for the seamounts is included in *SI Appendix*. Burger and Froude numbers are defined based on seamount height and diameter from ref. 31 and ambient stratification and velocity from refs. 34 and 35; see text for exact definitions and *SI Appendix* for further discussion and validation.

earlier studies of lee wave generation over generalized rough topography (44, 45). We also exclude the influence of tides, as we find that the tidal excursion is generally small compared to the horizontal scale of the seamounts, such that the tidal flows are likely to be secondary to the mean flow in the generation of wake vortices (*SI Appendix*). However, interactions between tides and seamounts can also be important for enhancing mixing (46, 47). Instead, our focus is on the turbulent mixing induced by vertically sheared layered vortices that form in the wake of seamounts throughout the world ocean, including potential secondary wave generation and trapping within the wake. To our knowledge, the basin-scale impacts of this regime of flow–seamount interaction have not been considered to date, yet, as we will see, these impacts are predicted to be important for global ocean circulation.

In Fig. 1C, we construct a map of  $Fr$  based on the KW11 seamount data and estimated values of stratification  $N$  and flow

speed  $U$ .  $N$  is estimated from climatological stratification (World Ocean Circulation Experiment; 48), taken at the nearest vertical level and horizontal grid point to the KW11 seamount mid-depths.  $U$  is also taken at the KW11 seamount mid-depths and is calculated from a field of root-mean-square flow speed from a  $1/48^\circ$  resolution ocean model simulation adapted from ref. 49 (LLC4320; see *Materials and Methods* and *SI Appendix*). The dependence of  $Fr$  on flow speed highlights regions associated with intense flows, such as the Antarctic Circumpolar Current (ACC), western boundary currents, abyssal channels and passages, etc. The corresponding estimate of  $Bu$  is displayed in Fig. 1E, illustrating that, overall, seamount wakes are expected to be more layered at low latitudes due to the inverse dependence of  $Bu$  on  $f$ —see also the distribution of seamounts in  $Fr - Ro$  space shown in *SI Appendix* Fig. S3. At high latitudes (e.g., in the ACC region), flow impingement on seamounts is instead mostly predicted to generate barotropic vortices. Note, however,

that substantial regional departures from this general pattern do occur, linked primarily to the seamount aspect ratio  $H/D$ .

A basin-by-basin histogram synthesis of the height to basal-depth (depth at the seamount base) ratio and  $Bu$  of the seamount field is provided by Fig. 1F. The Pacific Ocean stands out because it hosts larger percentages of high- $Bu$  and tall (relative to the local seafloor depth) seamounts than other basins. The more frequent occurrence of high- $Bu$  regimes makes the Pacific Ocean particularly favorable to developing shear-induced turbulence associated with layered wake vortices. In contrast, the Southern Ocean seamounts are expected to mostly produce barotropic vortices, with the Atlantic and Indian basins falling in between the Pacific and Southern Ocean extremes. The Pacific Ocean's comparative richness of "locally tall" seamounts further suggests that seamount-induced dynamics in this basin may impact shallower waters than in the rest of the world's oceans.

Given the strong dependence of the wake structure on the Rossby and Froude numbers, and following diapycnal diffusivity and energy dissipation scalings by Perfect et al. (42) and Srinivasan et al. (43), we look for a scaling for the diapycnal diffusivity due to the seamount wake of the form:  $K_\rho = K_1 Fr^\alpha Ro^\beta$ .

Based on idealized numerical simulations of the flow around an isolated seamount immersed in constant stratification, Perfect et al. (42) reported that the domain-averaged diapycnal diffusivity follows the scaling:

$$K_\rho^{(1)} \sim K_0 (Fr Ro)^2, \quad [1]$$

for  $N < 10^{-3} \text{ s}^{-1}$ , with  $K_0 \approx 3 \text{ m}^2 \text{ s}^{-1}$ . The size of their simulation (and averaging) domain is 2.6 seamount basal diameters in the cross-stream direction, 3.8 basal diameters in the along-stream direction and 1.4 seamount height in the vertical. According to this simple scaling, the vortex-associated diffusivity  $K_\rho^{(1)}$  may exceed background turbulent levels in the ocean interior ( $\sim 10^{-5} \text{ m}^2 \text{ s}^{-1}$ ) for  $Fr Ro \geq 0.002$ , and can be as large as mixing rates in the most energetic tidal zones ( $\geq 10^{-3} \text{ m}^2 \text{ s}^{-1}$ ) for  $Fr Ro \geq 0.02$  (50). The scaling of Eq. 1 exhibits qualitative consistency with results from a recent numerical study of equatorial topographic wakes (43). However, it was developed within highly idealized scenarios and its quantitative predictive power might not encompass the diversity of realistic oceanographic regimes.

An alternative scaling is obtained here using high-resolution realistic models of the ocean circulation in three paradigmatic regions: an equatorial area (representing the large- $Bu$  limit with strongly sheared, layered topographic vortices); a low-latitude area over the Mid-Atlantic Ridge (including a wide range of seamounts and  $Bu$ ); and a mid-latitude case, in the seamount-rich area around the New England Seamount Rise (representing  $Bu$  just above unity; see *Materials and Methods* and *SI Appendix* for a detailed description of the simulations). We derive this scaling by using a nonlinear least squares fit of the function  $K_\rho = K_1 Fr^\alpha Ro^\beta$  to the modeled diffusivities from the three high-resolution realistic models (suitably averaged around seamounts and excluding the deepest 100 m; see *SI Appendix*). Note that this fit was performed after selecting seamounts that meet the validity criteria of Eq. 1, which include  $Bu > 1$ ,  $Fr < 1$ , and  $Ro < 1$ , to focus on wake vortex regimes. The result is a function:

$$K_\rho^{(2)} \sim K_1 Fr^{1.7} Ro^{1.1}, \quad [2]$$

with  $K_1 = 0.6 \text{ m}^2 \text{ s}^{-1}$ . An interesting difference between the two scalings is the dependence on  $Ro$ , which is almost linear in Eq. 2 but quadratic in Eq. 1. This is an empirical result and (much) further research is required to fully understand the geophysical fluid dynamics of this problem.

Next, we assess the preceding theoretical framework and the validity of the two diapycnal diffusivity scaling relations by analyzing the seamount wakes and resulting diapycnal diffusivity in the three aforementioned high-resolution simulations, each corresponding to a typical dynamical regime. We will then apply the two scaling relations for the diapycnal diffusivity to the KW11 seamount data (Fig. 1B) and climatological stratification and flow speed data (Fig. 1C and E) to assess the contribution of seamount-induced mixing to deep-ocean upwelling on a global scale.

**Equatorial Seamounts: An Example of Layered Vortices.** The validity of the theoretical description of flow around a seamount in a realistic high- $Bu$  setting is first illustrated with a regional simulation in the equatorial Atlantic Ocean (Fig. 2; see *Materials and Methods* and *SI Appendix* for a detailed description of the simulation). Snapshots of relative vorticity at a vertical level (2,800 m) intersected by seamounts (Fig. 2A) and along a vertical section crossing the model domain (Fig. 2B) reveal the occurrence of intense cyclonic and anticyclonic filaments and vortices in the wake of the seamounts, following a predominantly southeastward current below 1,500 m (Movie S1). These features exhibit complex, vertically layered structures associated with intense vertical shear (Fig. 2E) and are thus expected to generate strong turbulent mixing. That the simulated wake vortices conform to theoretical predictions may be illustrated by estimating the set of dimensionless parameters on which the theory is founded. The modeled flows around the seamounts are characterized by a typical Rossby number  $Ro \sim 1$ , a Froude number  $Fr \sim 0.01 - 0.1$ , and a Burger number  $Bu \sim 100 - 10,000$ . These correspond squarely to the layered wake vortex regime (Fig. 1D) and thereby indicate that the area should have a rich field of layered topographic vortices (43)—as indeed it is found to.

The simulation also supports the notion that seamounts can elevate bulk regional deep-ocean diffusivities by one order of magnitude or more (Fig. 2D). Specifically, the vertically sheared layers in the simulation give rise to high diffusivities of as much as  $O(10^{-3} \text{ to } 10^{-2}) \text{ m}^2 \text{ s}^{-1}$  in the wakes of seamounts (Fig. 2F and G). These diffusivities exceed background mixing rates by one to two orders of magnitude below 1,500 m depth (Fig. 2D) and are in the range of diffusivities predicted by the theoretical scaling (Fig. 2C). A comprehensive comparison of modeled and scaling-predicted diffusivities is provided in *SI Appendix*.

**Mid-Atlantic Ridge and New England Seamounts: Examples of Hybrid Dynamics.** The Mid-Atlantic Ridge hosts seamounts with diverse radii, heights, and depths, thus spanning a wide range of  $Bu$  values (Fig. 1E). A regional simulation of a portion of the Mid-Atlantic Ridge extending from 5°S to 12°S is used here to illustrate a seamount wake regime that is a hybrid of coherent and layered vortex regimes (Fig. 3; see *Materials and Methods* and *SI Appendix* for a detailed description of the simulation). The impingement of mesoscale eddies on the seamounts generates a complex field of wake vortices, as revealed by a map of relative vorticity at 2,800 m (Fig. 3A; see also Movie S2). A vertical section of relative vorticity further shows that these vortices can be vertically coherent in the interior yet highly sheared in the vicinity of topography (Fig. 3D). A vertical view of the modeled

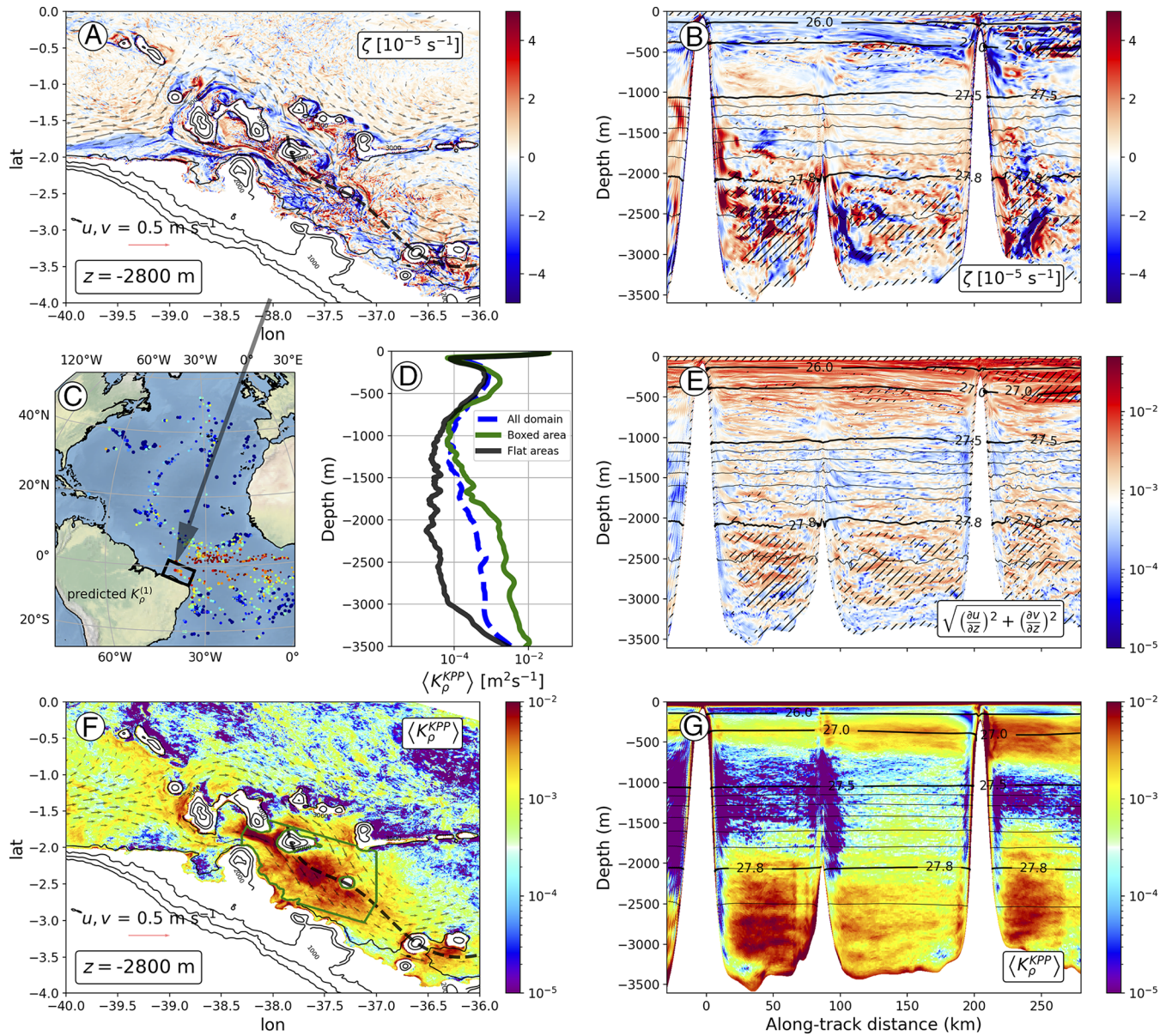


**Fig. 2.** (A and B) Snapshots of relative vorticity (A) at 2,800 m depth in the equatorial Atlantic Ocean, and (B) along an approximately along-stream vertical section crossing several seamounts (shown as a dashed line on panel A). Hatched regions highlight instantaneous vertical mixing coefficient  $K_p^{KPP}$  larger than  $10^{-4} \text{ m}^2 \text{ s}^{-1}$ . (C) Predicted vertical mixing coefficient  $K_p^{(1)}$  ( $\text{m}^2 \text{ s}^{-1}$ ) based on Eq. 1 and the seamount database following the color scale of panels F and G. The simulation domain is shown in black. (D) Vertical profiles of  $K_p^{KPP}$  ( $\text{m}^2 \text{ s}^{-1}$ ) spatially integrated over the full simulation domain in blue, over the seamount region in green (see green domain in panel F), and over a region away from seamounts in black. (E) Snapshot of vertical shear of horizontal velocity along the same along-stream vertical section as in (panel B). (F and G) Time-averaged vertical mixing coefficient  $K_p^{KPP}$  ( $\text{m}^2 \text{ s}^{-1}$ ) (F) at 2,800 m depth, and (G) along the same along-stream vertical section as in (panels B and E).

diapycnal diffusivity distribution indicates that turbulent mixing is enhanced within a few hundred meters of the seafloor or more around the wake vortices (Fig. 3H), with diffusivities approaching and exceeding  $O(10^{-3}) \text{ m}^2 \text{ s}^{-1}$  tens of kilometers around seamounts.

Cases with moderate  $Bu$  may also produce intense mixing. For example, numerical simulations of the New England seamounts—a chain of deep seamounts on the path of the Gulf Stream—highlight the occurrence of intense turbulent wakes and high-amplitude lee waves in the lee of the seamounts (Fig. 3 B and E). These wakes can extend horizontally up to 100 km downstream and vertically from the bottom to slightly above the peak of the seamounts. The seamount shown in

Fig. 3E has a shape similar to that of the idealized seamount studied by Perfect et al. (42), with characteristic values of  $D = 25 \text{ km}$  for the half-width,  $H = 3,000 \text{ m}$  for the height, and a background seafloor depth of 5,000 m. Locally, the Coriolis parameter is  $f \sim 0.8 \times 10^{-4} \text{ s}^{-1}$ , and the mean stratification is  $N \sim 10^{-3} \text{ s}^{-1}$ , corresponding to a typical Rossby number  $Ro \sim 0.1$ , a Froude number  $Fr \sim 0.1$ , and a Burger number  $Bu \sim 2$ . The vortical wake structure is thus expected to be more vertically coherent than in the previous cases, as confirmed by the simulation (Movie S3). The vortical wake is associated with an enhancement of turbulent mixing, again by one to two orders of magnitude relative to typical levels at the same depth away from the seamounts (Fig. 3I). In this case, the elevated diffusivities

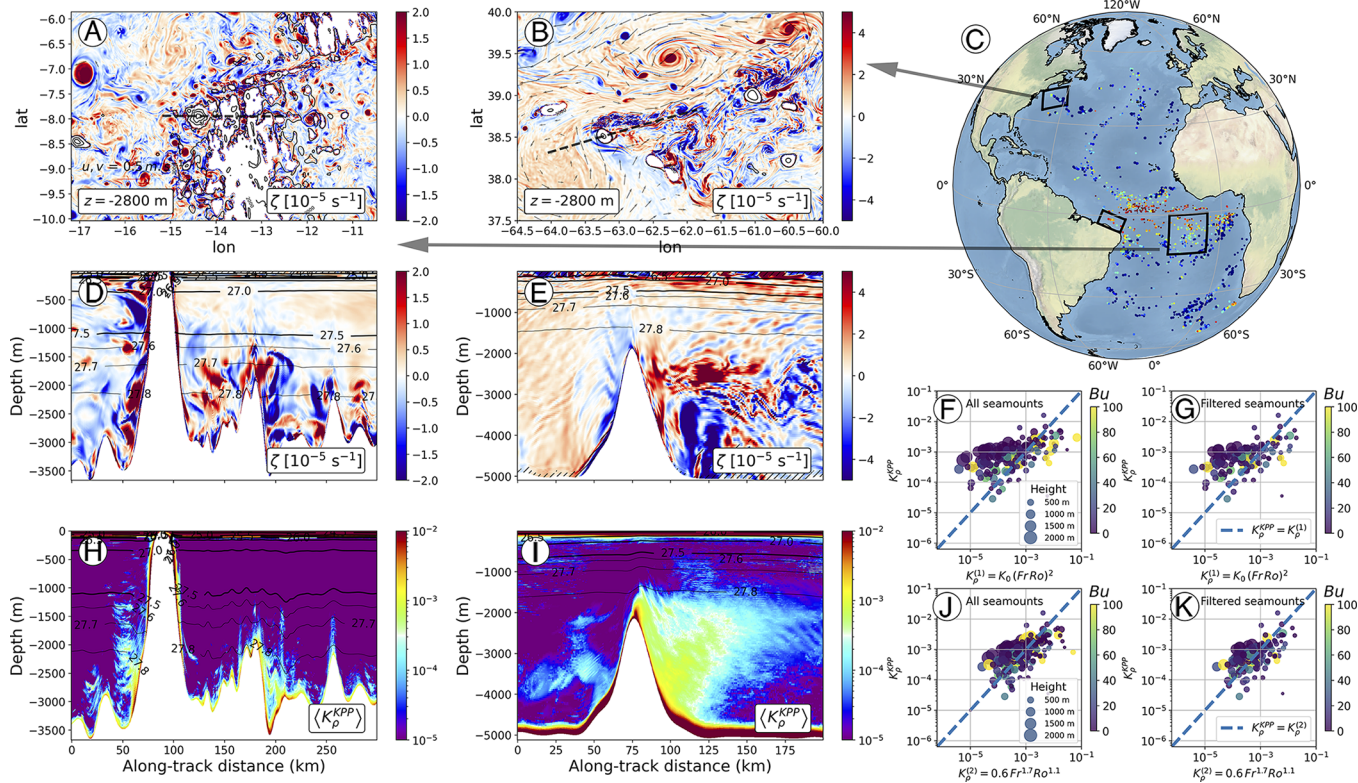


**Fig. 3.** (A and B) Snapshots of relative vorticity at 2,800 m depth (A) over the Mid-Atlantic ridge, and (B) in the North Atlantic. (C) Predicted diffusivity  $K_p^{(1)}$  ( $\text{m}^2 \text{s}^{-1}$ ) based on Eq. 1 and the seamount database, following the color scale of panels H and I. The simulation domains are shown in black. (D and E) Snapshots of relative vorticity along vertical sections crossing several seamounts (D) over the Mid-Atlantic ridge, and (E) in the North Atlantic (shown as dashed lines in panels A and B, respectively). Hatched regions highlight instantaneous diapycnal diffusivities  $KKPP$  larger than  $10^{-4} \text{ m}^2 \text{s}^{-1}$ . (F) Scatterplots of modeled diffusivities against predicted diffusivities based on the scaling  $K_p^{(1)} = K_0(\text{Fr Ro})^2$  (predictions based on model parameters) for all seamounts included in the three high-resolution simulation domains shown in panel (C). (G) Same as (F) using only seamounts included in the global computation (SI Appendix). (H and I) Time-averaged diffusivity  $K_p^{KPP}$  ( $\text{m}^2 \text{s}^{-1}$ ) along the same vertical sections as in (D and E). (J and K) Same as (F and G) using the scaling based on a nonlinear least squares fit of the model diffusivities:  $K_p^{(2)} = K_1 \text{Fr}^{1.7} \text{Ro}^{1.1}$  with  $K_1 = 0.6 \text{ m}^2 \text{s}^{-1}$ . The fit was derived using only seamounts included in the global computation; diffusivity is averaged over a cylinder surrounding each seamount and excluding the deepest 100 m of the water column (SI Appendix).

are localized predominantly on the anticyclonic side of the wake, as is characteristic of centrifugal instability in the near wake for extratropical cases with  $\text{Ro} < 1$  (43), but also show the signature of internal waves generated by the unstable wake and/or trapped inside by the anticyclonic side of the wake.

In all these examples, the theoretical scaling from Eq. 1 predicts diffusivities that display a wider range of values, with lower diffusivities for most seamounts and higher diffusivities for some high- $Bu$  seamounts (SI Appendix Fig. S12 and Fig. 3 F and G). On the other hand, the scaling from Eq. 2 shows a better agreement for seamounts in the low and moderate  $Bu$  regimes (Fig. 3 J and K), for which the model diffusivities were underestimated by the scaling of Eq. 1, and predicts smaller diffusivities than Eq. 1 for Rossby numbers of order one. A detailed comparison of modeled and scaling-predicted diffusivities is provided in SI Appendix. Although neither scaling fully captures mixing variability across seamounts, their endorsement by purposeful (idealized or realistic) numerical simulations authorizes their use in constructing baseline climatologies of seamount-generated mixing.

## Global Deep-Ocean Mixing and Upwelling

We explore the global implications of seamount-induced mixing by applying Eqs. 1 and 2 to the KW11 dataset and climatological hydrographic data. Specifically, we only account for the turbulence induced by the shear and instabilities in the seamount wake

( $Bu > 1$ ), which is currently absent from representations of ocean turbulence in climate models, and not the mixing associated with seamount-radiated internal lee waves or (internal tide or lee) wave–vortex interactions, which can have overlaps with existing mixing estimates. The outcome of our global diagnostics is shown in Fig. 4A—the details of the map’s construction are discussed in Materials and Methods and SI Appendix, where we describe the filtering process employed to ensure that the map produces a conservative mixing estimate while complying with the limitations of Eqs. 1 and 2. For comparison, we also show in Fig. 4 C and D estimates of the diffusivity induced by internal tides (50, 51) and lee waves radiated by abyssal hills (52) along an illustrative abyssal density surface (see SI Appendix for details). Seamount-generated mixing is found to be intense compared to the most energetic tidal and lee wave mixing, especially at lower latitudes, although strong tidal mixing is substantially more widely spread. We stress that the parameterized seamount mixing here only includes the contribution of layered wake vortices and thus excludes tidal or lee wave mixing induced by seamounts. This means there is no overlap between Fig. 4 A, C, and D, and in theory, lee wave mixing from seamounts is not present in either. The map in Fig. 4A is presently absent from mixing parameterizations in ocean and climate general circulation models.

The impact on deep-ocean upwelling of seamount-generated mixing is assessed by quantifying the rate of water mass transformation (53) generated by this and other (i.e., internal

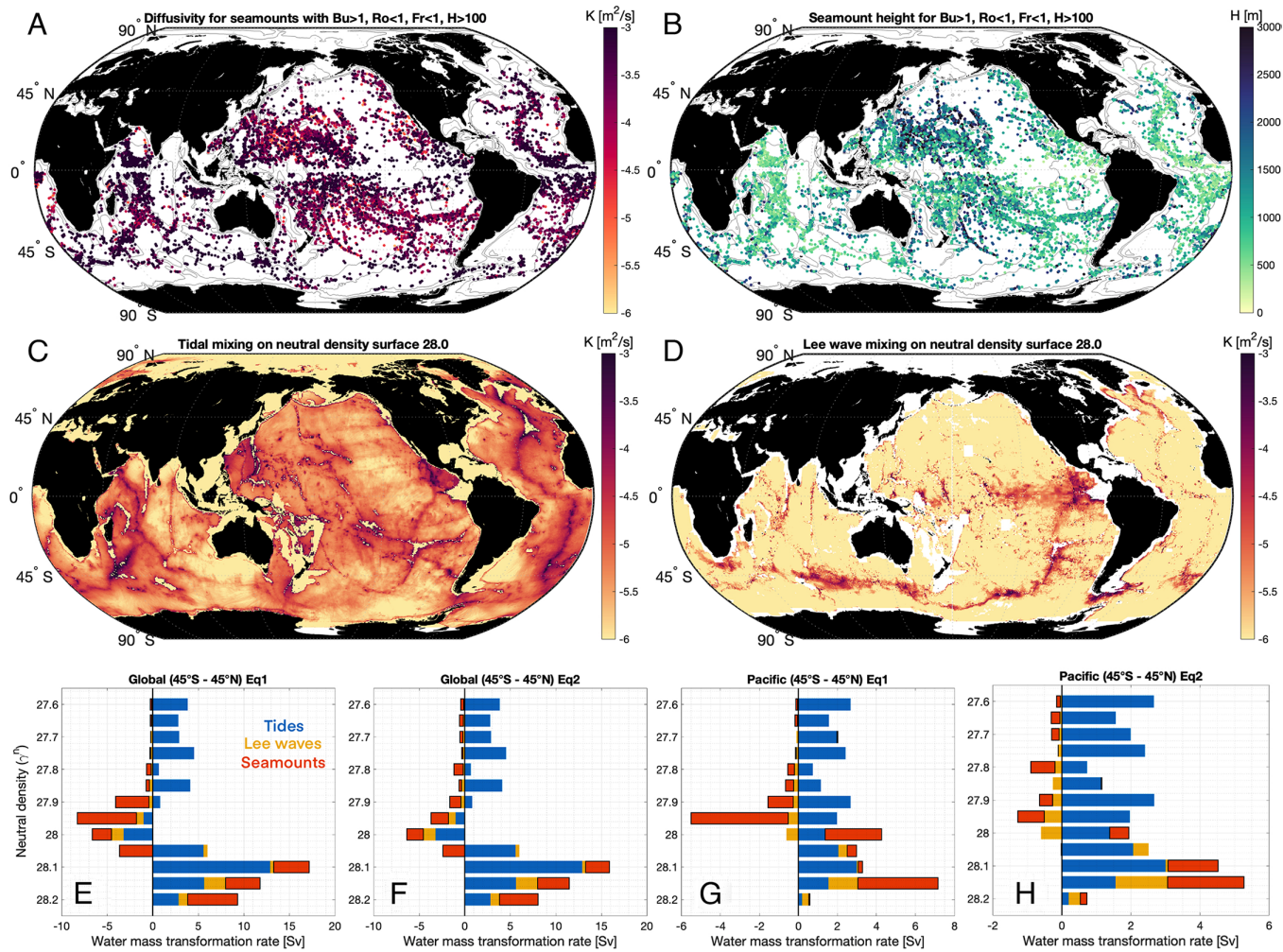


**Fig. 4.** (A) Distribution of seamounts expected to give rise to shear-induced turbulence associated with layered vortices in their wakes ( $Bu > 1$ ). Seamounts with  $Ro > 1$  (too close to the equator and not accounted for in Eq. 1),  $Fr > 1$  (for which flow is primarily directed over rather than around the seamount), and  $H < 100 \text{ m}$  (fully or partially within the turbulent bottom boundary layer) are all discarded (compare with maps shown in Fig. 1). The color shading indicates the effective turbulent diffusivity ( $\log_{10}$  scale) representing the mixing around and over the height of seamounts, as per Eq. 1. (B) Seamount heights for the seamounts in panel (A). (C) Diapycnal diffusivity ( $\log_{10}$  scale) from tidal mixing on a deep density surface of  $28 \text{ kg m}^{-3}$  with a mean depth of  $2,000 \text{ m}$  and mean height above the bottom of  $2,160 \text{ m}$  (from 50). Diffusivity on a deeper density surface,  $28.1 \text{ kg m}^{-3}$ , is shown in *SI Appendix*. (D) Diapycnal diffusivity ( $\log_{10}$  scale) from lee wave mixing on the same density surface as in panel (C) (from 57). (E–H) Water mass transformation rate in the  $45^\circ\text{S}$  to  $45^\circ\text{N}$  global ocean (E and F) and in the  $45^\circ\text{S}$  to  $45^\circ\text{N}$  Pacific Ocean (G and H). We focus on the ocean equatorward of  $45^\circ$  to exclude regions where nonlinearities of the equation of state would modify transformation rates significantly (1). In each panel, the net water mass transformation is decomposed into the contributions of (blue) internal tides, (red) seamounts, and (yellow) lee waves. Panels (E and G) show contribution due to seamounts calculated based on Eq. 1 and panels (F and H) show the same calculated based on Eq. 2. The former method often yields a larger contribution due to the larger diffusivities associated with high- $Bu$  and  $Ro \sim 1$  flows.

tides and lee waves) mixing agents. The outcome is shown in Fig. 4 E–H. As found by other recent works (1, 2, 54, 55), the net upwelling is the residual of downwelling (prevalent in the interior of basins) and upwelling (focused along topographic boundaries).

Examination of the individual contributions of seamount-, internal tide-, and lee wave-generated turbulence to the water mass transformation rate reveals that seamount-induced mixing is a significant player in the net global- or basin-scale diapycnal transfers. For some deep ( $>2 \text{ km}$ ) density classes, seamount-generated mixing contributes O(40%) or larger of the transformation; the tidal component is, of course, expected to be dominant (1, 55). The Pacific Ocean, in particular, seems to host a disproportionately large number of seamounts that can generate layered turbulence (Figs. 1F and 4A). As a result, seamount mixing is plausibly of leading-order importance for the deep Pacific circulation (Fig. 4 G and H). Like lee wave-driven mixing

(1), the presently estimated seamount mixing causes net buoyancy gain (hence upwelling) within abyssal density classes and net buoyancy loss (downwelling) within overlying layers (Fig. 4F).

We note that the goal of Fig. 4 E–H is not to provide a predictive measure of seamount mixing but to show its significant contribution, benchmarked against the much better studied and understood tidal mixing. Much more extensive research and observations are needed before seamount mixing can be accurately quantified on a global scale. Regional observational evidence of energetic turbulent mixing in seamount wakes is currently emerging (56). We suggest that a first step forward would be a comprehensive and accurate identification of seamounts based on recent advancements in seafloor mapping and machine learning methods. The vertical structure of seamount-generated dissipation and mixing also needs scrutiny to go beyond the simple step-like vertical diffusivity profile employed in our global maps (Fig. 4A and *SI Appendix*).

We emphasize that our estimates are conservative due to three factors: i) the seamount count of KW11 is very conservative; for example, all three of our regional case studies included many seamounts missing from KW11; ii) we only accounted for a small fraction of the known seamounts (e.g., compare Fig. 4A with Fig. 1B; see *SI Appendix*); other seamounts also contribute to mixing; and iii) we only accounted for shear-induced turbulence in between layered vortical wakes; seamounts are expected to produce additional mixing via wave generation, wave–vortex interactions, near-boundary instabilities, and tide-seamount interactions, none of which were accounted for here. Furthermore, we restricted the seamount mixing estimates to a narrower volume around the seamounts than one could expect based on our simulations or those upon which Eq. 1 was based.

## Conclusions

We have demonstrated that theoretical descriptions of turbulence generated by flow impingement on seamounts, which were developed under highly idealized scenarios, hold broadly for realistic flow and topography configurations. By conservatively applying these theoretical ideas to global seamount and oceanographic datasets, we have shown that turbulence associated with seamount-generated layered vortices makes an important contribution to deep-ocean mixing and upwelling—comparable to contributions from other, much more extensively studied sources of turbulence. We conclude that seamount-induced turbulence may be a significant player in the ongoing debate around the closure of the overturning circulation’s deep upwelling limb (8, 30, 58–65). This appears particularly plausible near the equator and in the subtropics, where the layered vortex regime highlighted in our work occurs widely.

Despite this regime’s likely important role in shaping the deep ocean circulation, to our knowledge, there have been no observations of seamount-generated layered vortices and their associated mixing to date. As such, the mixing effects of seamounts are absent from state-of-the-art climate-scale ocean models. Further, one of the largest uncertainties in the estimates presented here is the potentially significant underestimate in the number of seamounts; thus, future improvements to global bathymetric maps will play an important role in quantifying seamount-driven mixing. We suggest that addressing these major knowledge gaps will require not only first-of-their-kind observations (with the deep Pacific as a favored first candidate, given the expected importance of seamounts in this region) but also advances in dynamical understanding of the evolution of the separated vortices. This evolution may implicate a variety of instabilities (15, 16, 27, 43), as well as interactions with both submesoscale motions at the bottom boundary (17–20) and internal waves (24, 39). Ultimately, integrated measures and parameterizations of mixing accounting for these interacting phenomena are called for to faithfully represent seamount-generated turbulence in climate models.

## Materials and Methods

**Velocity Data from the LLC4320 Model.** Average flow speeds at the mid-heights of seamounts in the KW11 census are calculated from the LLC4320 model, a global, full-depth ocean and sea ice simulation carried out using the Massachusetts Institute of Technology general circulation model (MITgcm).

The model has  $1/48^\circ$  horizontal resolution (0.75 km near Antarctica, 2.3 km at the Equator, and 1 km in the Arctic Ocean) and 90 vertical levels, and has the highest resolution of a hierarchy of simulations that are initialized from a  $1/6^\circ$  global ocean state estimate from the Estimating the Circulation and Climate of the Ocean, Phase II, (ECCO2) output (49). The model partially resolves the seamounts of interest here—further discussion of the impact of this and details of the averaging procedure are provided in *SI Appendix*. Model descriptions can be found in refs. 34 and 66, and model data are available from the Estimating the Circulation and Climate of the Ocean (ECCO) data portal (<https://data.nas.nasa.gov/ecco/data.php>).

**Regional Models.** The three high-resolution regional simulations are performed using the Coastal and Regional Ocean Community model (CROCO), which is built upon the Regional Oceanic Modelling System (67). It solves the free surface, hydrostatic, and primitive equations using terrain-following vertical coordinates. The Equatorial domain covers an area of 900 km by 525 km with a horizontal grid spacing of 750 m and 300 vertical levels. The Mid-Atlantic Ridge domain spans an area of 1,500 km by 1,500 km with a horizontal grid spacing of 1 km and 300 vertical levels. The Gulf Stream domain covers an area of 1,000 km by 800 km with a horizontal grid spacing of 500 m and 256 vertical levels. All three domains are initialized and forced at their boundaries using the Atlantic-wide simulation GIGATL3 (68), a realistic simulation spanning the entire Atlantic Basin, performed also using CROCO with a horizontal grid spacing of 3 km and 100 vertical levels during the period 2004 to 2014. The regional simulations herein correspond to February 2008 to September 2008. The time-mean variables are computed using the last 6 mon of the simulations. Further details on the model simulations are provided in *SI Appendix*.

**Global Map of Seamount Diffusivity.** To construct mixing maps based on the layered seamount wake vortices, we first filtered the KW11 data to keep only seamounts with predicted layered dynamics. Estimated diffusivities at each seamount (Fig. 4A) were computed using the scaling for volume-averaged diffusivity reported in ref. 42 (Eq. 1), as well as the scaling obtained by fitting diffusivities from the high-resolution realistic simulations described above (Eq. 2), and applied over a cylinder of radius  $3L$ , where  $L$  is the basal radius, and height equal to that of the seamount. The filtering of seamounts and choice of volume are explained further in *SI Appendix*.

**Water Mass Transformation.** To calculate the water mass transformation rates presented in Fig. 4 E–H, we used the seamount diffusivities to construct a 2D “map” of mixing on the seafloor on a  $0.5^\circ$  (approximately 50 km) resolution latitude-longitude grid. For each 2D cell, the total mixing was calculated as the sum of that due to all the qualifying seamounts within the cell. We volume-weighted the diffusivity in each bin by multiplying it by the ratio of the seamount-induced mixing volume and the total cell volume. The mean height of the qualifying seamounts within a cell was also calculated. The 2D map was then translated into a 3D map on the same grid as the WOCE global hydrographic climatology (48): the total mixing in each basal 2D grid cell projected upward using a tanh profile, which is one from the seafloor to a height above the bottom equal to the mean seamount height within the cell and is zero above that. This 3D map of diffusivity was then used with WOCE gridded hydrography to derive water mass transformation rates following ref. 2 (see *SI Appendix* for more detail).

**Data, Materials, and Software Availability.** The LLC4320 data used to obtain velocities and stratification around seamounts were accessed via the ECCO Data Portal ([https://data.nas.nasa.gov/ecco/eccodata/lle\\_4320/](https://data.nas.nasa.gov/ecco/eccodata/lle_4320/)) (69) using the llereader of the xmitgcm Python package (70). Tidal mixing maps are available at <https://doi.org/10.17882/73082> (71). The seamount parameters calculated based on the LLC4320 and KW11 data are available at <https://zenodo.org/doi/10.5281/zenodo.11145851> (72); seamount diffusivities shown in Fig. 4 can be obtained from this dataset using Eqs. 1 and 2.

**ACKNOWLEDGMENTS.** A.M. acknowledges support from the UK Natural Environment Research Council grant NE/P018319/1 and from the Office of Naval Research grant N00014-22-1-2082. J.G. acknowledges support from the French National Agency for Research (ANR) through the project Deeper (ANR-19-CE01-0002-01), from the Partnership for Advanced Computing in Europe (PRACE) and the Grand Equipement National de Calcul Intensif (GENCI) for awarding access to computing resources Joliot-Curie Rome and skylake from GENCI-TGCC (Grants 2022-A0090112051, 2021-A0090112051, 2020-A0090112051, 2019gch0401, and PRACE project 2018194735), and from computing facilities Datarmor of “Pôle de Calcul Intensif pour la Mer” at Ifremer, Brest, France. L.E.B. was supported by EPSRC grants EP/L016613/1 and EP/X028135/1, and computational resources provided by the Imperial College London Research Computing Service are gratefully acknowledged (<https://doi.org/10.14469/hpc/2232>). J.J.R. acknowledges support from the Office of Naval Research, Grant N00014-19-1-2154. C.d.L. acknowledges

support from the French national LEFE programme through the ROOF project.

Author affiliations: <sup>a</sup>Department of Earth Sciences, University of Cambridge, CB2 3EQ, Cambridge, United Kingdom; <sup>b</sup>University of Western Brittany, CNRS, Institut de recherche pour le développement (IRD), Ifremer, Laboratoire d’Océanographie Physique et Spatiale, Institut Universitaire Européen de la Mer, F29280, Plouzané, France; <sup>c</sup>Institut Universitaire de France, 75231, Paris, France; <sup>d</sup>School of Mathematics, University of Edinburgh, EH9 3FD, Edinburgh, United Kingdom; <sup>e</sup>Ocean and Earth Science, University of Southampton, SO14 3ZH, Southampton, United Kingdom; <sup>f</sup>Department of Applied Mathematics and Theoretical Physics, University of Cambridge, CB3 0WA, Cambridge, United Kingdom; <sup>g</sup>University of Washington, Seattle, WA 98195; and <sup>h</sup>Laboratoire d’Océanographie et du Climat: Expérimentations et Approches Numériques (LOCEAN), Sorbonne Université-CNRS-Institut de recherche pour le développement (IRD), Muséum National d’Histoire Naturelle, 75005, Paris, France

Author contributions: A.M., J.G., A.C.N.G., and J.J.R. designed research; J.G. performed the numerical simulations; L.E.B. analyzed the seamount dataset; A.M. and C.d.L. constructed the global mixing maps; L.C. analyzed the global water mass transformation; A.M., J.G., L.E.B., A.C.N.G., L.C., J.J.R., and C.d.L. analyzed the results; and A.M., J.G., L.E.B., A.C.N.G., L.C., J.J.R., and C.d.L. wrote the paper.

1. C. De Lavergne, G. Madec, J. Le Sommer, A. G. Nurser, A. C. N. Garabato, On the consumption of Antarctic bottom water in the abyssal ocean. *J. Phys. Oceanogr.* **46**, 635–661 (2016).
2. R. Ferrari, A. Mashayek, T. J. McDougall, M. Nikurashin, J. M. Campin, Turning ocean mixing upside down. *J. Phys. Oceanogr.* **46**, 2239–2261 (2016).
3. S. E. M. Fletcher *et al.*, Inverse estimates of anthropogenic CO<sub>2</sub> uptake, transport, and storage by the ocean. *Global Biogeochem. Cycles* **20**, GB2002 (2006).
4. A. J. Watson, G. K. Vallis, M. Nikurashin, Southern ocean buoyancy forcing of ocean ventilation and glacial atmospheric CO<sub>2</sub>. *Nat. Geosci.* **8**, 861–864 (2015).
5. M. Nikurashin, G. K. Vallis, A theory of the interhemispheric meridional overturning circulation and associated stratification. *J. Phys. Oceanogr.* **42**, 1652–1667 (2012).
6. A. F. Thompson, A. Stewart, T. Bischoff, A multi-basin residual-mean model for the global overturning circulation. *J. Phys. Oceanogr.* **46**, 2583–2602 (2016).
7. H. F. Drake, R. Ferrari, J. Callies, Abyssal circulation driven by near-boundary mixing: Watermass transformations and interior stratification. *J. Phys. Oceanogr.* **50**, 2203–2226 (2020).
8. W. Munk, C. Wunsch, Abyssal recipes II: Energetics of tidal and wind mixing. *Deep-Sea Res.* **45**, 1977–2010 (1998).
9. C. B. Whalen *et al.*, Internal wave-driven mixing: Governing processes and consequences for climate. *Nat. Rev. Earth Environ.* **1**, 606–621 (2020).
10. K. L. Polzin, T. J. McDougall, “Mixing at the ocean’s bottom boundary” in *Ocean Mixing: Drivers Mechanisms Impacts*, M. Meredith, A. Naveira Garabato, Eds. (Elsevier BV, 2021), pp. 145–180.
11. L. Armi, Some evidence for boundary mixing in deep ocean. *J. Geophys. Res. Oceans* **83**, 1971–1979 (1978).
12. L. Armi, Some evidence for boundary mixing in deep ocean - Reply. *J. Geophys. Res. Oceans* **84**, 5097–5098 (1979).
13. M. H. Alföld *et al.*, Turbulent mixing and hydraulic control of abyssal water in the Samoan passage. *Geophys. Res. Lett.* **40**, 4668–4674 (2013).
14. L. Clément, A. M. Thurnherr, Abyssal upwelling in mid-ocean ridge fracture zones. *Geophys. Res. Lett.* **45**, 2424–2432 (2018).
15. M. Molemaker, J. C. McWilliams, W. Dewar, Submesoscale instability and generation of mesoscale anticyclones near a separation of the California Undercurrent. *J. Phys. Oceanogr.* **45**, 613–629 (2015).
16. J. Gula, M. Molemaker, J. C. McWilliams, Topographic generation of submesoscale centrifugal instability and energy dissipation. *Nat. Commun.* **7**, 12811 (2016).
17. J. O. Wenegrat, L. N. Thomas, Submesoscale baroclinic instability in the bottom boundary layer. *J. Phys. Oceanogr.* **48**, 2571–2592 (2018).
18. A. C. Naveira Garabato *et al.*, Rapid mixing and exchange of deep-ocean waters in an abyssal boundary current. *Proc. Natl. Acad. Sci. U.S.A.* **116**, 13233–13238 (2019).
19. J. O. Wenegrat, L. N. Thomas, Centrifugal and symmetric instability during Ekman adjustment of the bottom boundary layer. *J. Phys. Oceanogr.* **50**, 1793–1812 (2020).
20. J. Gula, J. Taylor, A. Shcherbina, A. Mahadevan, *Ocean Mixing: Drivers, Mechanisms and Impacts* (Elsevier BV, 2022), pp. 181–214.
21. J. C. McWilliams, Submesoscale currents in the ocean. *Proc. R. Soc. A* **472**, 20160117 (2016).
22. C. Vic *et al.*, Eddy-topography interactions and the fate of the Persian Gulf outflow. *J. Geophys. Res. Oceans* **120**, 6700–6717 (2015).
23. W. Dewar, M. Molemaker, J. C. McWilliams, Centrifugal instability and mixing in the California Undercurrent. *J. Phys. Oceanogr.* **45**, 1224–1241 (2015).
24. T. Nagai *et al.*, The Kuroshio flowing over seamounts and associated submesoscale flows drive 100-km-wide 100–1000-fold enhancement of turbulence. *Commun. Earth Environ.* **2**, 170 (2021).
25. C. Z. Lazaneo, P. H. R. Calil, A. Tandon, I. C. A. da Silveira, Submesoscale coherent vortices in the south Atlantic ocean: A pathway for energy dissipation. *J. Geophys. Res. Oceans* **127**, e2020JC017099 (2022).
26. B. Perfect, N. Kumar, J. J. Riley, Vortex structures in the wake of an idealized seamount in rotating, stratified flow. *Geophys. Res. Lett.* **45**, 9098–9105 (2018).
27. K. Srinivasan, J. C. McWilliams, M. J. Molemaker, R. Barkan, Submesoscale vortical wakes in the lee of topography. *J. Phys. Oceanogr.* **49**, 1949–1971 (2019).
28. P. Wessel, D. T. Sandwell, S. S. Kim, The global seamount census. *Oceanography* **23**, 24–33 (2010).
29. C. Yesson, M. R. Clark, M. L. Taylor, A. D. Rogers, The global distribution of seamounts based on 30 arc seconds bathymetry data. *Deep Sea Res. Part I* **58**, 442–453 (2011).
30. Q. Cao *et al.*, Seamount-induced mixing revealed through idealized experiments and its parameterization in an oceanic general circulation model. *Deep Sea Res. Part II* **202**, 105144 (2022).
31. S. S. Kim, P. Wessel, New global seamount census from altimetry-derived gravity data. *Geophys. J. Int.* **186**, 615–631 (2011).
32. J. Gevorgian, D. T. Sandwell, Y. Yu, S. S. Kim, P. Wessel, Global distribution and morphology of small seamounts. *Earth Space Sci.* **10**, e2022EA002331 (2023).
33. J. A. Goff, B. K. Arbic, Global prediction of abyssal hill roughness statistics for use in ocean models from digital maps of paleo-spreading rate, paleo-ridge orientation, and sediment thickness. *Ocean Model.* **32**, 36–43 (2010).
34. C. B. Rocha, T. K. Chereskin, S. T. Gille, D. Menemenlis, Mesoscale to submesoscale wavenumber spectra in drake passage. *J. Phys. Oceanogr.* **46**, 601–620 (2016).
35. B. K. Arbic *et al.*, “2018: A primer on global internal tide and internal gravity wave continuum modeling in HYCOM and MITgcm” in *New Frontiers in Operational Oceanography*, E. Chassaignet, A. Pascual, J. Tintoré, J. Verron, Eds. (GODAE OceanView, 2018), pp. 307–392.
36. J. Gula, T. M. Blaćić, R. E. Todd, Submesoscale coherent vortices in the Gulf Stream. *Geophys. Res. Lett.* **46**, 2704–2714 (2019).
37. D. C. Napolitano, I. C. A. da Silveira, A. Tandon, P. H. R. Calil, Submesoscale phenomena due to the brazil current crossing of the vitória-trindade ridge. *J. Geophys. Res. Oceans* **126**, e2020JC016731 (2021).
38. R. B. Smith, Mountain-induced stagnation points in hydrostatic flow. *Tellus A* **41**, 270–274 (1989).
39. B. Perfect, N. Kumar, J. J. Riley, Energetics of seamount wakes. Part II: Wave fluxes. *J. Phys. Oceanogr.* **50**, 1383–1398 (2020).
40. M. Wurtel, R. Sharman, A. Datta, Atmospheric lee waves. *Annu. Rev. Fluid Mech.* **28**, 429–476 (1996).
41. R. B. Smith, 100 years of progress on mountain meteorology research. *Meteorol. Monogr.* **59**, 20.1–20.73 (2019).
42. B. Perfect, N. Kumar, J. J. Riley, Energetics of seamount wakes. Part I: Energy exchange. *J. Phys. Oceanogr.* **50**, 1365–1382 (2020).
43. K. Srinivasan, J. C. McWilliams, A. Jagannathan, High vertical shear and dissipation in equatorial topographic wakes. *J. Phys. Oceanogr.* **51**, 1985–2001 (2021).
44. M. Nikurashin, R. Ferrari, Global energy conversion rate from geostrophic flows into internal lee waves in the deep ocean. *Geophys. Res. Lett.* **38**, L08610 (2011).
45. A. C. N. Garabato, A. J. G. Nurser, R. B. Scott, J. A. Goff, The impact of small-scale topography on the dynamical balance of the ocean. *J. Phys. Oceanogr.* **43**, 647–668 (2013).
46. E. Kunze, J. M. Toole, Tidally driven vorticity, diurnal shear, and turbulence atop fieberling seamount. *J. Phys. Oceanogr.* **27**, 2663–2693 (1997).
47. P. Puthan, G. Pawlak, S. Sarkar, Wake vortices and dissipation in a tidally modulated flow past a three-dimensional topography. *J. Geophys. Res. Oceans* **127**, e2022JC018470 (2022).
48. V. Gouretski, K. P. Koltermann, WOCE global hydrographic climatology. *Berichte des BSH* **35**, 1–52 (2004).
49. D. Menemenlis *et al.*, Ecco2: High resolution global ocean and sea ice data synthesis. *Mercator Ocean Quart. Newslet.* **31**, 13–21 (2008).
50. C. de Lavergne *et al.*, A parameterization of local and remote tidal mixing. *J. Adv. Model. Earth Syst.* **12**, e2020MS002065 (2020).
51. C. de Lavergne *et al.*, Global tidal mixing maps. *SEANOE* **10**, 73082 (2020).
52. M. Nikurashin, R. Ferrari, Global energy conversion rate from geostrophic flows into internal lee waves in the deep ocean. *Geophys. Res. Lett.* **38**, L08610 (2011).
53. S. Goeskamp *et al.*, The water mass transformation framework for ocean physics and biogeochemistry. *Ann. Rev. Mar. Sci.* **11**, 271–305 (2019).
54. A. Mashayek *et al.*, Efficiency of turbulent mixing in the abyssal ocean circulation. *Geophys. Res. Lett.* **44**, 6296–6306 (2017).
55. L. Cimoli *et al.*, Sensitivity of deep ocean mixing to local internal tide breaking and mixing efficiency. *Geophys. Res. Lett.* **46**, 14622–14633 (2019).
56. A. Takahashi *et al.*, Energetic stratified turbulence generated by Kuroshio-seamount interactions in Tokara strait. *J. Phys. Oceanogr.* **54**, 461–484 (2023).
57. M. Nikurashin, R. Ferrari, Overturning circulation driven by breaking internal waves in the deep ocean. *Geophys. Res. Lett.* **40**, 3133–3137 (2013).
58. L. D. Talley, J. L. Reid, P. E. Robbins, Data-based meridional overturning streamfunctions for the Global ocean. *J. Clim.* **16**, 3213–3226 (2003).
59. C. Wunsch, R. Ferrari, Vertical mixing, energy, and the general circulation of the oceans. *Annu. Rev. Fluid Mech.* **36**, 281–314 (2004).
60. R. Lumpkin, K. Speer, Global ocean meridional overturning. *J. Phys. Oceanogr.* **37**, 2550–2562 (2007).
61. L. Talley, Closure of the Global overturning circulation through the Indian, Pacific, and Southern Oceans: Schematics and transports. *Oceanography* **26**, 80–97 (2013).
62. A. F. Waterhouse *et al.*, Global patterns of diapycnal mixing from measurements of the turbulent dissipation rate. *J. Phys. Oceanogr.* **44**, 1854–1872 (2014).

63. R. Ferrari, Oceanography: What goes down must come up. *Nature* **513**, 179–180 (2014).
64. T. Huussen, A. Naveira-Garabato, H. Bryden, E. McDonagh, Is the deep Indian ocean MOC sustained by breaking internal waves? *J. Geophys. Res. Oceans* **117**, C08024 (2012).
65. L. Cimoli *et al.*, Significance of diapycnal mixing within the Atlantic Meridional overturning circulation. *Nat. Commun.* **4**, e2022AV000800 (2021).
66. Z. Su, J. Wang, P. Klein, A. F. Thompson, D. Menemenlis, Ocean submesoscales as a key component of the global heat budget. *Nat. Commun.* **9**, 1–8 (2018).
67. A. Shchepetkin, J. C. McWilliams, The Regional Oceanic Modeling System (ROMS): A split-explicit, free-surface, topography-following-coordinate ocean model. *Ocean Model.* **9**, 347–404 (2005).
68. J. Gula, S. Theetten, G. Carbon, G. Roullet, Description of the GIGATL simulations. Zenodo. <https://zenodo.org/records/4948523>. Deposited 14 June 2021.
69. D. Menemenlis, LLC4320, NASA ECCO Data Portal. [https://data.nas.nasa.gov/ecco/eccodata/llc\\_4320/](https://data.nas.nasa.gov/ecco/eccodata/llc_4320/). Accessed 1 December 2022.
70. R. P. Abernathey *et al.*, xmitgcm: Read MITgcm mds binary files into xarray. Zenodo. <https://doi.org/10.5281/zenodo.596253>. Deposited 27 July 2021.
71. C. de Lavergne, Global tidal mixing maps. SEANOE. <https://doi.org/10.17882/73082>. Deposited 2 April 2020.
72. L. Baker, Seamount parameters used in Mashayek & Gula *et al.* PNAS 2024 [Data set]. Zenodo. <https://doi.org/10.5281/zenodo.11145852>. Deposited 8 May 2024.